





Dynamics of quantum solitons in Lee-Huang-Yang spin-orbit-coupled Bose-Einstein condensatesSonal Gangwar ¹, Rajamanickam Ravisankar ^{1,2}, Paulsamy Muruganandam ³, and Pankaj Kumar Mishra ^{1,*}¹*Department of Physics, Indian Institute of Technology, Guwahati 781039, Assam, India*²*Institute of Atomic and Molecular Sciences, Academia Sinica, Taipei 10617, Taiwan*³*Department of Physics, Bharathidasan University, Tiruchirappalli 620024, Tamilnadu, India*

(Received 15 September 2022; accepted 5 December 2022; published 20 December 2022)

We present the numerical results of the structure and dynamics of the self-bound ground state arising solely because of the presence of beyond-mean-field quantum fluctuation in spin-orbit- (SO-) coupled binary Bose-Einstein condensates in one dimension. We obtain an analytical soliton solution for nonzero SO coupling that matches quite well with the numerical results. Further, we investigate the dynamical stability of these solitons by adopting three protocols, such as (i) adding initial velocity to each component, (ii) quenching the SO- and Rabi-coupling parameters at initial and finite time, and (iii) allowing collision between the two spin components by giving equal and opposite direction velocity to them. For small velocity perturbation, the soliton has the presence of the breathing oscillation, while large velocity perturbations transform the soliton into moving solitons. The maximum breathing frequency exhibits power-law dependence on the Rabi-coupling frequency with an exponent ~ 0.16 . The quenching of SO and Rabi couplings results in several interesting dynamical features, such as dynamical phase transition from plane to stripe phase, dynamical flipping of the spin state, and secondary solitonic modes. In the absence of the SO and Rabi couplings, depending upon the velocity of the up- and down-spin components, the collision between them is either elastic or inelastic, which is consistent with the earlier numerical and experimental observations. However, in the presence of coupling parameters, the collision appears to be inelastic and quasielastic in nature.

DOI: [10.1103/PhysRevA.106.063315](https://doi.org/10.1103/PhysRevA.106.063315)**I. INTRODUCTION**

An exciting aspect of weakly interacting Bose-Einstein condensates (BECs) is the appearance of a self-bound quantum droplet state that results from the balance between the attractive force due to the mean-field interaction and repulsive force due to quantum fluctuation [1–3]. One can theoretically model the contribution of the quantum fluctuations by considering the beyond-mean-field (BMF) term, popularly known as the Lee-Huang-Yang (LHY) correction, in the mean-field Hamiltonian of the condensate [4]. BMF terms were corroborated first time in experiments with homogeneous and single-component Bose gas of ^{85}Rb [5] and ^7Li [6], and recently in binary ^{39}K [7]. In a binary mixture, the quantum droplet in three dimensions manifests in a spherical shape due to the competition between the effective short-range attractive interaction between the atoms and the repulsive interaction arising solely due to the BMF, which is also responsible for its stabilization [3]. In general, the LHY correction term is attractive in quasi-one dimension, while it is repulsive in two and three dimensions [1,3].

The advancement in the state-of-art technology and simulation tools in ultracold BECs led to an upsurge in the research in quantum droplets during the past few decades. The quantum droplet was first reported experimentally in the dipolar BECs, for which a single-component dipolar BEC made of dysprosium (^{164}Dy) produced elongated quantum droplets in one direction [8–10]. Chomaz *et al.* observed similar features with

the condensate of erbium atoms (^{166}Er) [11]. Subsequently, several groups realized quantum droplets in binary mixtures of isotropic BECs [12–15], Bose-Fermi mixture [16], and also in binary magnetic gases [17]. These quantum droplets are commonly observed in three dimensions, while it is possible to increase the lifetime of the droplets in the lower dimensions. The formation of one-dimensional quantum droplets is due to the balance between the repulsive mean-field (MF) contribution to the energy per particle, which is linear in the density (n) of the gas, and the attractive BMF correction, proportional to $-n^{1/2}$ [1,2].

Since the proposition of the nontrivial attractive nature of the LHY term in quasi-one-dimensional quantum droplet [2], it has caught the great attention of the scientific community. A significant number of experimental [18] as well as theoretical and numerical works have been performed in recent years using the effective one component [19], binary [20], and spin-orbit- and Rabi-coupled binary BECs [21,22] that explored the structure and dynamics of the quantum droplet. Tononi *et al.*, in SO-coupled BECs, demonstrated that the self-bound states are solitonic in nature for vanishing mean-field contribution [21]. Depending upon the Rabi- and SO-coupling parameter ranges, these solitonlike states are either of single-peak (bright soliton) or multiple-peak (stripe soliton) nature [21,23]. Some of these works demonstrate the existence of soliton and droplet nature of the self-bound state for the effective one-component binary BECs in one dimension [24] as well as in the binary mixture with SO coupling in two dimensions [22,25]. The transition between the quantum soliton and quantum droplet regimes depends on several parameters,

*pankaj.mishra@iitg.ac.in

like the atom number (N), interaction strength, the strength of the confining potential, etc. [24]. For large N , a highly dense droplet solution exists, while low dense bright soliton occurs for small N [19]. A recent experiment shows that the attractive mixture of BECs confined in an optical waveguide could exhibit both quantum soliton and quantum droplets. At large N , the droplet exhibits similar characteristics as those of the classical droplets [13].

Although lots of emphasis on exploring the structure and stability of quantum droplets in the recent past, only a limited number of works are available in the literature that focus on the dynamical aspect of quantum droplets. Ferioli *et al.* analyzed the dynamics of quantum droplets in a binary mixture by allowing the droplets to collide with each other [15]. In classical droplet collisions, there are two possibilities, either they merge into a single one, or the colliding droplets separate two or more ones after collision [26]. Ferioli *et al.* have investigated the collision between the quantum droplets by experimental and numerical means for the binary mixture of hyperfine states in ^{39}K and found the merging and separation between the droplets depending on their velocity. Critical velocity for the transition between the elastic and inelastic collision strongly depends upon the atom number N [15]. A few theoretical studies are available that establish the robustness of the quantum soliton or quantum droplet during the collision. For instance, Astrakharchik and Malomed numerically investigated the static and dynamical properties of quantum droplets using the mean-field theory and studied the collision properties of two counterpropagating droplets [19]. They showed that collisions between the tiny droplets are quasielastic, indicating solitonic behavior. While depending on the velocity, the large droplets may undergo merging or fragmentation, which shows the collision as inelastic. Recently, Young and Adhikari numerically studied the collision properties of bright solitons in two-dimensional dipolar BECs [27].

In recent years, one may witness numerous theoretical and numerical works focusing on the structure and dynamics of the droplets in binary BECs. However, only a few studies are available on the droplets in the spinor BECs, especially in spin-orbit-coupled binary BECs [21,28]. In particular, the role of SO- and Rabi-coupling parameters in dictating the shape and dynamics of the quantum droplet is not well understood. In this paper, we present a detailed numerical investigation to understand the effect of the SO- and Rabi-coupling parameters on the stability and shape of the quantum soliton. Although Tononi *et al.* [21] demonstrate the presence of the self-bound quantum soliton due to the LHY term with vanishing mean-field contributions, several aspects, like dynamical robustness of the ground state for different perturbations, have not been explored yet. In this paper, we have performed a systematic analysis of the effect of initial velocity, quenching of the SO- and Rabi-coupling parameters, and allowing the collision between the components by initially perturbing the components with equal and opposite speeds. All these protocols facilitate us to obtain a variety of dynamical phases that include breathing (both in space and time), repelling, multifragmented solitons, etc.

The structure of our paper is as follows. In Sec. II, we present governing equations and numerical simulation details and outline a possible scenario to connect our numerical

parameters with the experiment. We illustrate an analytical solution of the ground state of the quantum soliton in the presence of SO coupling in Sec. III. Following this in Sec. IV, we present a detailed analysis of the ground-state structure followed by its dynamics which are set up in the system by different procedures. First, we discuss the different sorts of dynamics that arise due to the initial velocity given to the soliton, followed by the dynamics due to the quenching of coupling parameters. Further, we highlight some of the pronounced dynamical behavior shown by the solitons in the presence of collisions. Finally, we conclude our work in Sec. V.

II. BEYOND-MEAN-FIELD MODEL FOR SO-COUPLED BECs

We consider a pseudo-spin- $\frac{1}{2}$ Bose-Einstein condensate confined in strong transverse confinement modeled using quasi-one-dimensional spin-orbit- and Rabi-coupled condensates with LHY term. The corresponding coupled Gross-Pitaevskii (GP) equations in dimensionless form are given by [21]

$$i\partial_t\psi_\uparrow = \left[-\frac{1}{2}\partial_x^2 - ik_L\partial_x + g|\psi_\uparrow|^2 + g_{\uparrow\downarrow}|\psi_\downarrow|^2 - \frac{g_{\text{LHY}}^{3/2}}{\pi}\sqrt{|\psi_\uparrow|^2 + |\psi_\downarrow|^2} \right] \psi_\uparrow + \Omega\psi_\downarrow, \quad (1a)$$

$$i\partial_t\psi_\downarrow = \left[-\frac{1}{2}\partial_x^2 + ik_L\partial_x + g_{\downarrow\uparrow}|\psi_\uparrow|^2 + g|\psi_\downarrow|^2 - \frac{g_{\text{LHY}}^{3/2}}{\pi}\sqrt{|\psi_\uparrow|^2 + |\psi_\downarrow|^2} \right] \psi_\downarrow + \Omega\psi_\uparrow, \quad (1b)$$

where ψ_\uparrow and ψ_\downarrow are the wave functions of the spin-up and -down components, respectively, k_L is the spin-orbit-coupling strength, Ω is the Rabi-coupling frequency, g is the intraspecies interaction, and $g_{\uparrow\downarrow}$ are the interspecies interaction strengths. We consider the interaction term due to the LHY correction as $g_{\text{LHY}} = g$. The wave functions are subjected to the following normalization condition:

$$\int_{-\infty}^{\infty} |\psi_\uparrow|^2 dx = \int_{-\infty}^{\infty} |\psi_\downarrow|^2 dx = 1, \quad (2)$$

which remains conserved with the time.

Equations (1) are nondimensionalized using transverse harmonic oscillator length $a_0 = \sqrt{\hbar/(m\omega_\perp)}$ as a characteristic length scale (where ω_\perp is the trap frequency in the transverse direction), ω_\perp^{-1} as a timescale, and $\hbar\omega_\perp$ as an energy scale. The other interaction parameters are considered as $g = 2Na_{\uparrow\uparrow}/a_0$ and $g_{\uparrow\downarrow} = 2Na_{\uparrow\downarrow}/a_0$. Here, $a_{\uparrow\uparrow}$ and $a_{\uparrow\downarrow}$ represent the scattering length corresponding to intracomponents and intercomponents, respectively. The SO- and the Rabi-coupling parameters have been rescaled as $k_L \rightarrow k_L a_0$ and $\Omega \rightarrow \Omega/\omega_\perp$, respectively, while the wave function is rescaled as $\psi_{\uparrow,\downarrow} = \psi_{\uparrow,\downarrow} \sqrt{a_0}$.

To make the numerical simulation experimentally viable, we choose the parameters same as considered in the recent realization of the quantum droplet in the binary hyperfine states mixture of ^{39}K condensates [12,13,15]. Following this we consider $N \sim 10^4$ atoms confined in the harmonic trap potential with frequencies $\omega_x = 2\pi \times 50$ Hz,

$\omega_{\perp} = 2\pi \times 800$ Hz in axial and perpendicular directions, respectively. Using this, the characteristic length scale can be obtained as $a_{\perp} \sim 0.6$ μm . Generally, in the experiment two internal hyperfine states $|F = 1, m_F = -1\rangle$ and $|F = 1, m_F = 0\rangle$ are considered which can be attributed, respectively, to the pseudo-spin-up $|\uparrow\rangle$ and pseudo-spin-down $|\downarrow\rangle$ states of our model. These two spin states have an equal number of atoms, and intraspecies and interspecies interaction strengths can be controlled by tuning s -wave scattering lengths through Feshbach resonance and by varying the magnetic field. Following the experiment we set $a_{\uparrow\uparrow} = a_{\downarrow\downarrow} = -a_{\uparrow\downarrow} = 0.2686a_0$ (a_0 is the Bohr radius) which gives the dimensionless interaction strengths as $g = g_{\text{LHY}} \approx 0.5$. Note that here we have taken all the scattering lengths to be the same to make the contribution of the mean-field term on the structure and dynamics of the soliton vanishingly small. However, the recent experiment on the quantum droplet with ^{39}K indicates the presence of soliton nature of the condensate is only possible when all the scattering lengths are not equal [13]. We expect our results will not alter much upon considering the unequal scattering lengths, as observed in the experiment. Another parameter in this system is the Rabi-coupling frequency (Ω), commonly used for coupling the spin states by tuning the frequency of Raman lasers ranging from $\Omega = 2\pi \times \{0.080\text{--}40\}$ kHz, which implies that the dimensionless Rabi-coupling frequency range as $\Omega = \{0.1, 50\}$. It is possible to vary the SO-coupling strength (k_L) with the laser wavelength and their geometry. In this work we have considered the dimensionless SO-coupling range $k_L = \{0.1, 8\}$, where the laser wavelength varies as $\lambda_L = 17.8$ μm –223.2 nm. Note that the LHY interaction is not equal to the MF interaction because the LHY nonlinear interaction term appears with an extra factor π . We have considered $g_{\text{LHY}} = g = 0.5$ and 1.0, for which the quantum fluctuation term contributes approximately of the order of 11% and 30%, respectively. Interestingly albeit of small contribution, we have obtained a large variety of dynamical features for our system without any confinement.

We employ the imaginary-time propagation method with the aid of a split-step Crank-Nicolson scheme [29–31] to numerically solve the coupled GP equations (1a) and (1b). The box size $[-153.6:153.6]$ with spatial resolution as $dx = 0.025$ is chosen for all the simulation runs, and we use the Gaussian initial condition with antisymmetric profiles on the components, i.e., $\psi_{\uparrow}(x) = -\psi_{\downarrow}(-x)$. The time step is fixed at $dt = 10^{-5}$. We also consider various interaction strength ($g = 0.5, 1, 2$) for our studies.

III. ANALYTICAL SOLITON SOLUTION

Here, we present the analytical solution of the ground state for our model. For brevity, we wish to obtain a solution for zero Rabi-coupling frequency ($\Omega = 0$) and finite k_L . For this purpose, we consider the following transformation to eliminate the SO-coupling term from Eq. (1):

$$\psi_{\uparrow}(x, t) = \tilde{\psi}_{\uparrow}(x, t) \exp\left[\frac{ik_L}{2}(k_L t - 2x)\right], \quad (3a)$$

$$\psi_{\downarrow}(x, t) = \tilde{\psi}_{\downarrow}(x, t) \exp\left[\frac{ik_L}{2}(k_L t + 2x)\right] \quad (3b)$$

Using the single field approximation we get $\tilde{\psi}_{\uparrow} = \tilde{\psi}_{\downarrow} = \phi(x) \exp(i\mu t)$. Based on the system parameters $g_{\uparrow\downarrow} = -g$, we find that the mean-field interaction term cancels each other, which yields the stationary state solution of the form

$$-\mu\phi = -\frac{1}{2}\partial_x^2\phi - \frac{\sqrt{2}}{\pi}g^{3/2}\phi^2 \quad (4)$$

which gives

$$\phi'^2 = \alpha\phi^2 - \beta\phi^3 \quad (5)$$

where the prime (') represents the spatial derivative with respect to x and $\alpha = 2\mu$, $\beta = 2\sqrt{2}g^{3/2}/3\pi$. Now the solution of Eq. (5) becomes [21]

$$\phi(x) = \phi(0) \operatorname{sech}^2(\sqrt{\mu/2} x), \quad (6)$$

where $\phi(0) = \alpha/\beta$. Here, the stationary state solution depends on the chemical potential. Using the normalization condition $\int |\psi_{\uparrow}|^2 dx = \int |\psi_{\downarrow}|^2 dx = 1$ we obtain $2|\mu| = (g^2/3^{2/3}\pi^{4/3})$. Thus, the final solution of Eq. (1) has the form as

$$\begin{aligned} \psi_{\uparrow} &= \left(\frac{\alpha}{\beta}\right) \operatorname{sech}^2\left(\sqrt{\frac{\mu}{2}} x\right) \exp\left[\frac{ik_L}{2}(k_L t - 2x) + i\mu t\right], \\ \psi_{\downarrow} &= \left(\frac{\alpha}{\beta}\right) \operatorname{sech}^2\left(\sqrt{\frac{\mu}{2}} x\right) \exp\left[\frac{ik_L}{2}(k_L t + 2x) + i\mu t\right]. \end{aligned} \quad (7)$$

In Fig. 1, we plot the analytical (red line) solution [Eqs. (7)] as well as numerical simulation (black dots) results of the stationary ground state of Eq. (1) for $g_{\text{LHY}} = g = 0.5$, with $\Omega = 0$ and $k_L = 1$. Both analytical and numerical simulation results match reasonably well for the real and imaginary parts and the total density of components.

In brief, we found the approximate soliton solution for the system of coupled Eqs. (1) by eliminating the SO-coupling term using the transformation with zero Rabi-coupling frequency. In the process, we have used single field approximation, which provides $\operatorname{sech}^2(x)$ soliton solution due to quadratic nonlinearity [21].

IV. NUMERICAL RESULTS

In this section, first, we present our numerical results for different ground-state solitons obtained using the imaginary-time propagation scheme. Our main emphasis is to ascertain the role of mean-field and beyond-mean-field LHY term on the overall shape and structure of the self-bound quantum soliton state. Following this, we focus on the soliton dynamics by employing the real-time propagation of the governing dynamical GP equations. Finally, we present a detailed analysis of the dynamics of quantum solitons by giving initial velocity, quenching the coupling parameters, and allowing the collision between the components by initially imparting them with an equal speed in the opposite direction.

A. Stationary ground states of quantum solitons

To better understand the role of the beyond-mean-field term (g_{LHY}) along with the SO- and Rabi-coupling frequency on the shape and size of the ground state, we now proceed

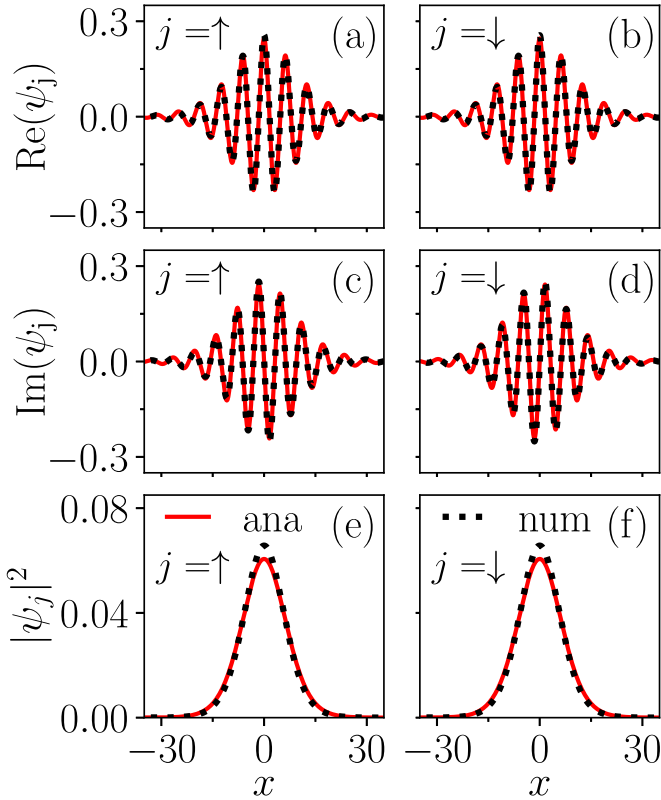


FIG. 1. A comparison between the numerically obtained soliton profiles (dotted black line) and analytical (solid red line) solution (7) for interaction strengths $g = 0.5$, and coupling parameters $k_L = 1$ and $\Omega = 0$. Real parts of the spin components: (a) $\text{Re}(\psi_\uparrow)$ and (b) $\text{Re}(\psi_\downarrow)$; imaginary parts of the spin components: (c) $\text{Im}(\psi_\uparrow)$ and (d) $\text{Im}(\psi_\downarrow)$; and the densities of the (e) up $|\psi_\uparrow|^2$ and (f) down $|\psi_\downarrow|^2$ components.

to get the different ground states of the solitons by assuming $g = -g_{\uparrow\downarrow} = g_{\text{LHY}}$. Here, we use MF and BMF acronyms to represent the ground states of the system in absence ($g_{\text{LHY}} = 0$) and presence of LHY correction ($g_{\text{LHY}} \neq 0$), respectively. In general, depending upon the coupling parameters' range, the ground states are either bright soliton (BS) or stripe soliton (SS) in nature [21,32].

We begin the analysis of the structure of BS in absence of g_{LHY} (labeled as MF) for the fixed parameters $k_L = \Omega = 1$ and $g = -g_{\uparrow\downarrow} = 0.5$. In Fig. 2(a), the solid black line represents the BS state. In the presence of g_{LHY} (labeled as BMF) magnitude of the BS gets doubled, and it tends to become more localized even though the width of the soliton appears to get reduced, as represented by the dashed red line in Fig. 2(a).

Further, upon increasing the interaction strengths to $g = -g_{\uparrow\downarrow} = 1$, we find a negligible change in the amplitude and width of the mean-field bright soliton (MF-BS) [see Fig. 2(b) (solid black line)]. However, in the presence of LHY interaction ($g_{\text{LHY}} = 1$) a well-localized quantum bright soliton (QBS) width gets reduced by half, while its amplitude is increased by a factor ≈ 2.66 [see Fig. 2(b) (dashed red line)].

Next, we consider the shape and structure of SS both in presence and absence of LHY correction term which was obtained for $\Omega = 1$ and $k_L = 4$ at $g = 0.5, 1$. A phase transition

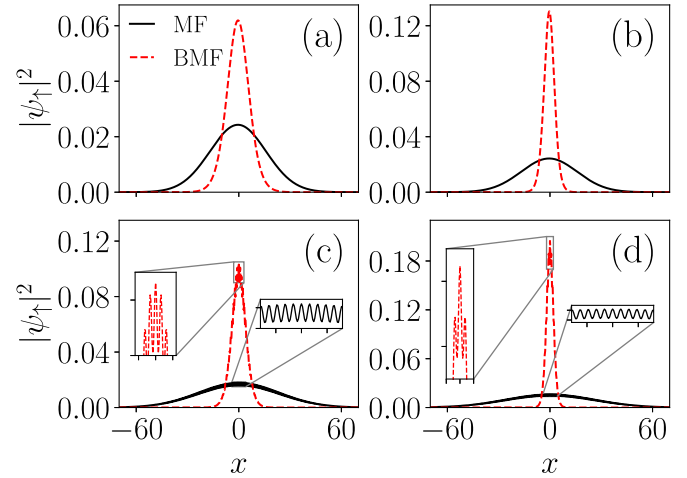


FIG. 2. Ground-state density profiles of the spin-up component in the presence and absence of LHY term. Bright soliton for $\Omega = 1$ and $k_L = 1$ with (a) $g = 0.5$ and (b) $g = 1.0$, and stripe soliton for $\Omega = 1$ and $k_L = 4$ with (c) $g = 0.5$ and (d) $g = 1.0$. The spin density gets more confined when the LHY term (dashed red line) is present. The insets in (c) and (d) show the magnified views of the stripe patterns in the presence and absence of the LHY term.

from BS to SS states occurs as we change the SO-coupling strength from $k_L = 1$ to 4. The fringes that appear in the density profiles characterize the stripe wave pattern. One may note that several local maxima appear in the density profile for both the MF and quantum solitons. In the presence of the LHY term with interaction strength $g = 0.5$, the number of stripes, as well as the width, gets reduced, and amplitude gets doubled compared to those without LHY, indicating the localization of the soliton [see Fig. 2(c)]. On increasing the interaction strength to $g = 1$, we find that the mean-field stripe soliton (MF-SS) [shown with the black line in Fig. 2(d)] exhibits similar nature as those for $g = 0.5$. However, the LHY-SS or quantum SS (QSS) phase width gets reduced by half, and an increase in the amplitude by a factor ≈ 4 , accompanied by a loss in the number of stripes and an increment in the localization [shown with the red line in Fig. 2(d)] is observed. Overall, we noticed that the condensate shape hardly changes upon increasing the MF interaction strengths. However, we note a significant change in the shape and amplitude when we consider the LHY correction ($g_{\text{LHY}} \neq 0$). With the LHY correction on increasing the nonlinear interaction (g), the size of the soliton gets reduced while the amplitude increases.

B. Dynamics of different phases of quantum soliton

In this section, we present the dynamics of the ground state of the MF and quantum soliton by solving the governing equation [cf. Eqs. (1)] with the help of real-time propagation. The main aim here is to investigate the dynamics of the MF and BMF quantum solitons by giving some initial velocity to the condensate by making a uniform change in the phase of the soliton wave function [21,33]. Further, we demonstrate the appearance of breathing solitons, fragmented soliton, free expansion of soliton, etc., by manipulating the magnitude of the initial velocity.

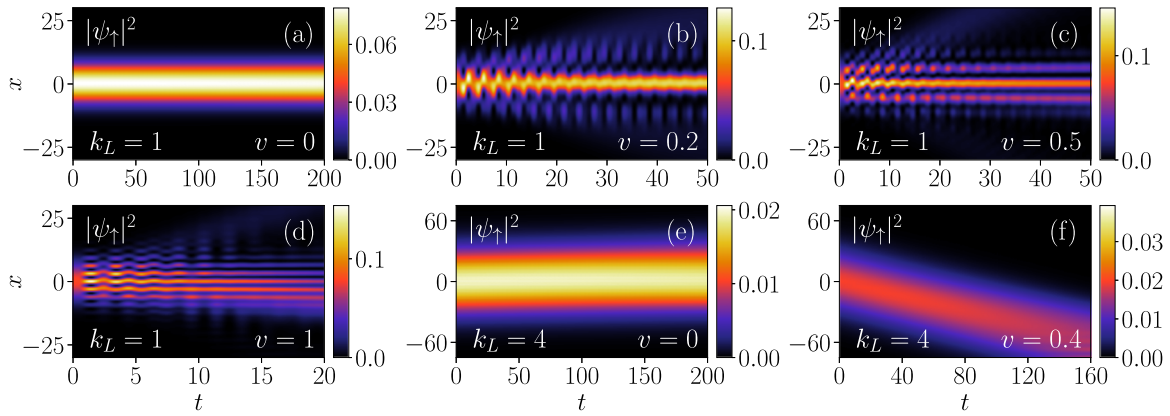


FIG. 3. Temporal evolution of mean-field (MF) bright soliton (BS) at different initial velocities: (a) $v = 0$, (b) $v = 0.2$, (c) $v = 0.5$, and (d) $v = 1$ for $g = -g_{\uparrow\downarrow} = 0.5$ and $\Omega = k_L = 1$. Upon increasing the velocity from $v = 0$ to 0.2 , a transition from the soliton to an oscillating soliton takes place. For large velocity multisolitons (at $v = 0.5$) and bifurcated solitons (at $v = 1$) are observed. Temporal evolution of MF stripe soliton for different velocities: (e) $v = 0$ and (f) $v = 0.4$ with $g = -g_{\uparrow\downarrow} = 0.5$, $\Omega = 1$, and $k_L = 4$. For $v = 0$ shape of the soliton remains unchanged until $t \sim 200$. For finite velocity ($v = 0.4$), the stripe soliton shows propagation along the initial velocity direction.

Figures 3(a)–3(d) depict the temporal evolution of BS for different velocities $v = 0, 0.2, 0.5$, and 1 , respectively, with $g = -g_{\uparrow\downarrow} = 0.5$ and $\Omega = k_L = 1$. For $v = 0$, the soliton propagates without any distortion [see Fig. 3(a)]. For a small but finite initial velocity (for example, $v = 0.2$), we notice setting up a time-dependent oscillation in the soliton that manifests as an undulating motion of the density in time and space. Beyond $t \sim 30$, the oscillation amplitude appears to vanish and a stable soliton is observed [cf. Fig. 3(b)]. This oscillation can be associated with the instability that soliton displays upon making a sudden change in the phase by a factor $\exp(\pm ivx)$, where v is the resultant acquired velocity. Note that up- and down-spin components of the condensates have been given negative and positive x -direction velocity, respectively. We also observe an expansion in the soliton upon waiting for a longer period. For $v = 0.5$, the soliton appears to display breaking into secondary solitons and breatherlike oscillation in which it exhibits expansion followed by compression at a periodic time interval [see Fig. 3(c)]. The spin component exhibits interesting dynamical behavior. We noticed the absence of the breather on one side while it is present on the other side. However, the middle lobe exhibits oscillation for a shorter time and expansion in a long duration indicates the presence of an oscillation deathlike behavior in the soliton [34]. In addition, we also observe the presence of multisoliton-like features. At $v = 1$, fragmented solitons with breatherlike modes get generated and propagate in the respective directions for the spin components, accompanied by the appearance of bifurcationlike multisolitons [cf. Fig. 3(d)].

We observe similar nature of dynamical behavior in the SS as those observed for BS in the absence of the LHY term. In Figs. 3(e) and 3(f), we show the temporal evolution of SS in the absence of LHY term for $\Omega = 1$ and $k_L = 4$ with $g = 0.5$ for (e) $v = 0$ and (f) $v = 0.4$. For $v = 0$, the SS state exhibits stripe solitonic feature. However, at higher velocity ($v = 0.4$), bifurcation of the stripe soliton into two propagating solitons occurs, which exhibits expansion with time.

After discussing the dynamics of the soliton in the presence of MF term only, we now analyze the dynamical evolution when we consider the BMF term along with MF term for both

QBS and QSS. In Fig. 4, we illustrate the dynamics of QBS with the BMF (i.e., with LHY correction term) for different initial velocities $v = 0, 0.5$ and $v = 1.0$ at $g = -g_{\uparrow\downarrow} = 0.5$ and $\Omega = k_L = 1$. For zero velocity the soliton exhibits stable nature with no change in its shape and size with time as depicted in Fig. 4(a): the feature is same as that for the MF bright soliton. On increasing the velocity to $v = 0.5$, the soliton displays breatherlike expansion and compression behavior at periodic intervals, as shown in Fig. 4(b). Here we find that the expansion of the condensate gets under control due to the presence of g_{LHY} interaction, stabilizing the expanding condensate without any trap. The frequency of these breather modes depends on the coupling parameters, which we shall discuss in detail in the later part of the paper. Note that Tononi *et al.* reported similar breatherlike soliton [21], which was attained by a slight perturbation in the width of the ground state. As we increase the initial velocity to $v = 1$, the soliton develops periodic breather oscillations and exhibits bifurcationlike features in which the center of the soliton moves in the $\pm x$ directions. Note that the up-spin component moves in the $-x$ direction while the other component moves in the $+x$ direction. This feature is noticeable for a finite time $t \lesssim 10$. Beyond this time, the breathers expand and span the entire space while the centered soliton exhibits expansion. Apart from this, we also notice that it exhibits bright-dark soliton for a shorter time, which finally gets converted into multisoliton at a longer period [19] as displayed in Fig. 4(c).

Further, we focus on the dynamics of QSS with LHY correction at different velocities $v = 0, 0.2$, and 1.0 for the parameters $g = -g_{\uparrow\downarrow} = 0.5$, $\Omega = 1$, and $k_L = 4$. At $v = 0$, QSS remains stable and maintains its shape and size for a longer duration [see Fig. 5(a)]. However, with finite velocity ($v = 0.2$) QSS propagates for a while in the $\pm x$ directions, thereafter, for $t \gtrsim 50$ they start displaying decaying (dilatation) feature until $t \lesssim 300$. Following this, the dilatation slowly gets diminished and for $t \gtrsim 500$ the soliton gets revived [see Fig. 5(b)]. The whole revival and expansion of the soliton with time is similar to those obtained for the QBS [see Fig. 4(b)]. For $v > 0.5$, the QSS evolves with time in the respective directions and, after

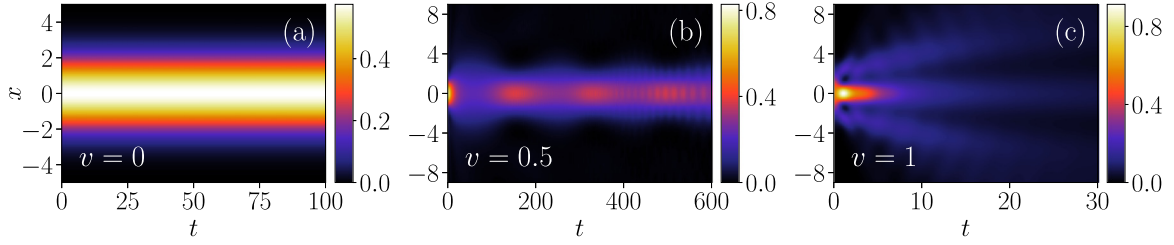


FIG. 4. Plots of the total density, $\sum_{j=\uparrow,\downarrow} |\psi_j|^2$, showing dynamics of quantum bright soliton (QBS) with LHY correction for $g = -g_{\uparrow\downarrow} = 0.5$, $\Omega = 1$, $k_L = 1$ at different velocities: (a) soliton propagates with no shape change for $v = 0$, (b) breathers for finite velocity $v = 0.5$, and (c) oscillation and bifurcation for $v = 1.0$. Increase in the velocity leads transitions from bright soliton to breather which further gets transformed into multisolitons.

separation, they do not combine again, as shown for $v = 1.0$ in Fig. 5(c).

Next, we analyze the dependence of the breathing frequency for the quantum soliton as observed in Figs. 4(b) and 5(b) on the SO- and Rabi-coupling parameters. We compute the breathing frequency (ω_{bf}) using the time series of the density oscillation of the soliton. In Fig. 6(a) we show dependence of ω_{bf} on the SO couplings (k_L) for various Ω when the soliton was assigned the initial velocity as $v = 0.1$. Following Ref. [21], here we consider the initial wave function as Gaussian, which is different than that of the exact solution of the ground state. The breathing frequency is around 0.025 for $k_L = 0$ for all values of Ω . At $\Omega = 0$ the ω_{bf} remains unchanged upon increasing k_L . For finite Rabi-coupling frequency ($\Omega = 1, 2, 4$), breather starts appearing at periodic intervals. For fixed Ω as $k_L^2 < \Omega$ the breathing frequency increases upon increasing in k_L . It attains the maximum at critical SO coupling ($k_L^2 = \Omega$) where the QBS to QSS phase transition occurs. For $k_L^2 > \Omega$, ω_{bf} decreases slowly in the regime of quantum stripe soliton. At higher k_L , ω_{bf} have the same value as those at $k_L \sim 0$ for all Ω . The critical breathing frequency (ω_{bf}^c) increases upon an increase in the Rabi frequency. Figure 6(b) illustrates the variation of ω_{bf} with k_L for different velocities $v = 0.1$ and 0.2 at $g = 0.5$. We have considered two sets of Rabi couplings $\Omega = 1$ and 4 for the analysis. The overall variation in ω_{bf} with k_L appears to be the same for both the velocities ($v = 0.1$ and 0.2), except that at lower velocity ($v = 0.1$) it has higher value compared to those at large velocity ($v = 0.2$). Interestingly, ω_{bf}^c remains the same for all the velocities ($v = 0.1$ and 0.2) as shown in Fig. 6(b), indicating that the breathing frequency at the critical point remains unchanged upon increasing the velocity. To better understand the dependence of the ω_{bf} on the interaction strengths

in Fig. 6(c) we show its variation with k_L for different g ($g = 0.5, 1.0, 2.0$) at $\Omega = 4$ and $v = 0.1$. We observe that the ω_{bf} for a given k_L shows increasing behavior on increasing the interaction strength. The critical SO coupling (k_L^c) and corresponding critical breathing frequency (ω_{bf}^c) also increase upon the increase in g .

In Fig. 7(a), we plot the variation of ω_{bf}^c with Ω for $v = 0.1$. We find that ω_{bf}^c shows power-law dependence on Ω with an exponent 0.16. In Fig. 7(b), we plot the variation of ω_{bf} with initial velocity for fixed Rabi coupling ($\Omega = 2$) and for two sets of SO couplings $k_L = 1.2$ (solid red line) and $k_L = 1.8$ (dashed blue line). Here, we notice that ω_{bf} decreases upon increasing the initial velocity for both the k_L . The fall in the breathing frequency with the velocity becomes sharper upon the increase in k_L . However, for a given initial velocity, the ω_{bf} is small for $k_L = 1.8$, which happens to be in QSS than those for $k_L = 1.2$ at which we have QBS ground state. We note that the chemical potential in the QBS regime does not change with k_L until $k_L < k_L^c$, which indicates that the soliton is energetically stable in the BS regime. On the other hand, when we increase the Rabi frequency Ω to 2, the critical k_L for the transition from the bright to stripe soliton also increases. Overall, we find that the ground-state energy of the quantum soliton gets lower upon increasing Ω for a given k_L , suggesting a better way of obtaining an energetically stable soliton.

Another notable feature is the transition of the breathing soliton phase into the moving soliton upon the increase in the velocity as depicted in Figs. 4 and 5. A similar feature of the soliton with increase in the velocity has been reported in Ref. [19] for the binary mixture with an assumption of symmetric behavior of the components. However, the presence of Rabi and SO coupling between the components makes the

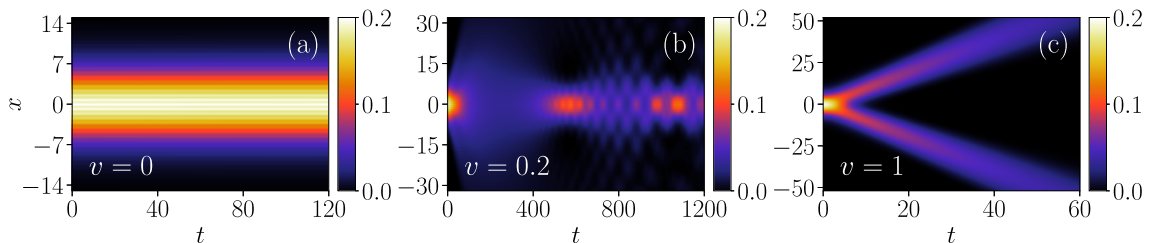


FIG. 5. Plots of the total density, $\sum_{j=\uparrow,\downarrow} |\psi_j|^2$, showing the dynamics of quantum stripe soliton (QSS) with LHY correction at different velocities: (a) $v = 0$, (b) $v = 0.2$, and (c) $v = 1.0$ for $g = -g_{\uparrow\downarrow} = 0.5$ and $\Omega = 1$, $k_L = 4$. For $v = 0$ stable stripe soliton is observed. However, for finite velocity breathers ($v = 0.2$) and bifurcated ($v = 1.0$) solitons are observed.

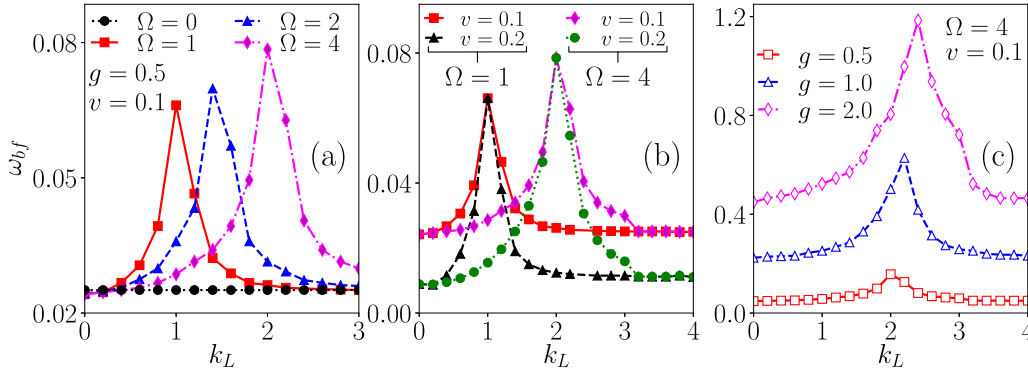


FIG. 6. (a) Variation of breathing frequency (ω_{bf}) with the SO-coupling strength (k_L) for different Ω with fixed velocity $v = 0.1$. (b) The variation of ω_{bf} with k_L for different Rabi coupling ($\Omega = 1, 4$) and velocities $v = 0.1, 0.2$ with $g = 0.5$. At the critical k_L where PW-SS phase transition happens, ω_{bf}^c remains independent of the velocity. (c) Variation of ω_{bf} with k_L for different interaction strengths $g = 0.5, 1.0, 2.0$ at $\Omega = 4$ and $v = 0.1$. To bring the graph to the same scale, we multiply the data for $g = 0.5$ and $g = 1.0$ by a factor of 2.

nature of these breathing and moving solitons more complicated here. We can understand the instability that leads to the transition from breathers to the moving soliton by looking at the SO, Rabi, and the kinetic part of the chemical potential. While the kinetic term varies as v^2 , the SO and Rabi parts will have linear and square dependence on the velocity, respectively. Due to this, one witnesses competition between the kinetic energy, which is positive and the SO and Rabi parts will have negative values upon changing the velocity. Overall, we expect the domination of the breathing soliton

region by the SO- and Rabi-coupling contributions, while the moving soliton region kinetic energy dominates. The above also indicates that the chemical potential attains minimum at the critical velocity, which is consistent with our numerical observation.

After analyzing the dynamics of the solitons by imparting an initial velocity, in the following section, we present different dynamical features arising due to making an instantaneous quench in the coupling parameters (Ω and k_L).

C. Quench dynamics of quantum soliton

To better understand the effect of the SO and Rabi couplings on the overall dynamics (without giving any initial velocity) of the quantum solitons, in this section we employ the instantaneous quench of the coupling parameters and analyze the resultant dynamics. With this protocol, we have obtained a variety of notable features like the generation of secondary and repulsive solitons, the dynamical phase transition from the QBS to the QSS and vice versa, etc.

In Fig. 8, we show the dynamical evolution of the soliton which generally arises due to the quench of Rabi-coupling frequency by fixing the interaction strength to $g = -g_{\uparrow\downarrow} = 0.5$. The ground-state soliton was initially prepared for $\Omega = 0, k_L = 2$. As we quench the Rabi frequency from $\Omega = 0 \rightarrow 1$ at finite time ($t \sim 20$) we notice that the QBS gets transformed to the QSS [see Figs. 8(a)–8(c)]. However, upon employing $\Omega = 0 \rightarrow 5$, the QBS phase of the soliton gets transformed into a phase that displays expansion and certain characteristics of the repulsive soliton as shown in Figs. 8(d)–8(f).

In Fig. 9, we show the dynamical evolution of the solitons for two kinds of quenching protocols: (a)–(c) when $\Omega = 0 \rightarrow 50$ and $k_L = 2 \rightarrow 4$ and (d)–(f) when $\Omega = 0 \rightarrow 50, k_L = 2 \rightarrow 8$. In the first case, we find the appearance of multisolitons with interferencelike patterns. Following the quenching, solitons get bifurcated into four that propagate away from each other and behave like repelling solitons. In the density profile, the outermost solitons show breathinglike features, and the innermost one inherits pure, stable solitonlike characteristics, i.e., they do not exhibit any change in shape and size with time as shown in Figs. 9(a)–9(c). For the second quenching protocol ($\Omega = 0 \rightarrow 50$ and $k_L = 2 \rightarrow 8$), again, multisoliton behavior appears, which has some differences

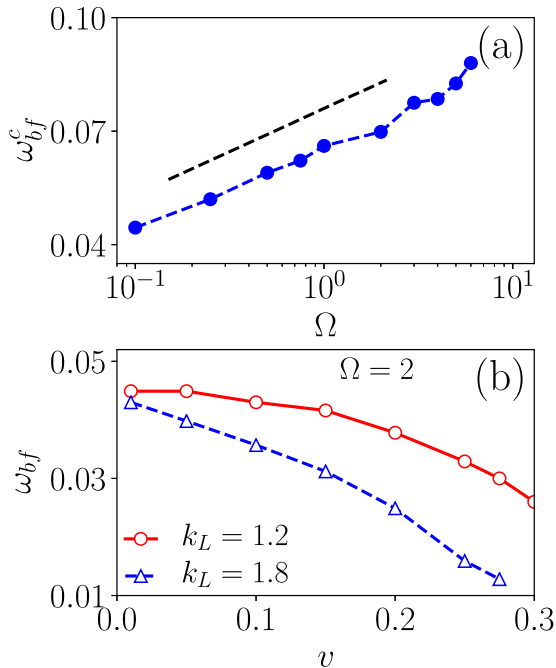


FIG. 7. (a) Variation of breathing frequency (ω_{bf}^c) at critical k_L with Ω for fixed velocity $v = 0.1$. The other parameters are the same as those in Fig. 6. The critical breathing frequency increases and exhibits power-law behavior with Ω as $\omega_{bf}^c \sim \Omega^{0.16}$. The dashed line is drawn as a guide to the eye to show the power-law nature of the ω_{bf}^c with Ω . (b) Variation of breathing frequency ω_{bf} with initial velocity v for different k_L keeping Rabi frequency fixed to $\Omega = 2$. The ω_{bf} is small for higher k_L for all the velocity.

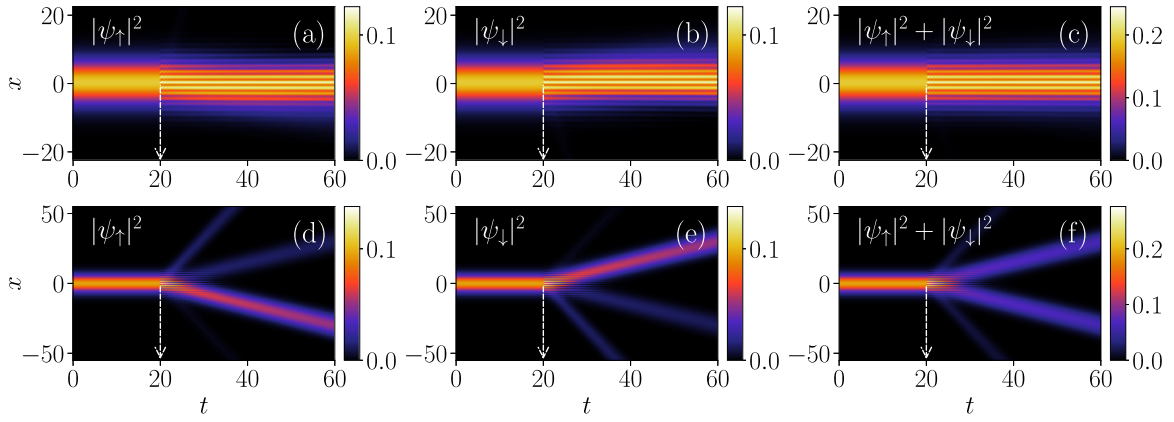


FIG. 8. Dynamics of the quantum soliton appearing due to different quenching protocols at $g = -g_{\uparrow\downarrow} = 0.5$ as it was initially prepared for $\Omega = 0, k_L = 2$. (a)–(c) When the Rabi frequency is quenched as $\Omega = 0 \rightarrow 1$ at $t = 20$, the initial QBS phase changes to QSS. (d)–(f) Quenching of Rabi frequency as $\Omega = 0 \rightarrow 5$ at $t = 20$ transforms the QBS phase into repulsive solitons.

compared to the previous case. For this case, we notice that the outermost soliton breather gets transformed into solitons with a relatively larger repulsive angle, while the innermost solitons transform into the stripe solitons and show attraction towards each other as depicted in Figs. 9(d)–9(f). Thus, quenching of the coupling parameters (either one of Rabi and SO or both simultaneously) leads to generation of secondary solitons. Similar types of secondary solitons have been noticed experimentally as an excitation of the bright matter wave solitons in quasi-one-dimensional geometry [35].

Next, we discuss the effect of double-quench protocols on the soliton dynamics. In Fig. 10, we show the dynamics of the quantum solitons as we implement double-quenching protocols [36] of the coupling parameters for the initial ground state prepared at $\Omega = 0, k_L = 2$ for $g = -g_{\uparrow\downarrow} = 0.5$. In Figs. 10(a)–10(c), we show the evolution when the first quench is performed by instantaneously switching off the SO coupling, that is, making the change $k_L = 2 \rightarrow 0$ at $t = 0$. Subsequently, we allow the soliton to evolve until $t = 20$ when we apply another quench by changing Rabi frequency as $\Omega = 0 \rightarrow 1$ and switching on the SO coupling as $k_L =$

$0 \rightarrow 2$. The first quenching, where we switch off the SO coupling, initially allows the solitons corresponding to the up and down components to display repulsive behavior and move in the space until the application of a second quenching. After the second quench ($\Omega = 0 \rightarrow 1, k_L = 0 \rightarrow 2$) at $t = 20$, we notice a switching off the soliton position from $x = 0$ to some finite value which further remains invariant with time. Overall, we see that the double-quench protocol provides more stability to the solitons. This particular feature is one of the promising potential applications for quantum information and quantum computing which is based on the mixing and demixing of qubits [37,38]. As we perform the first quenching the same as the previous case while in the second quench, only change in Rabi frequency is executed with $\Omega = 0 \rightarrow 5$ at $t = 10$ we find the appearance of moving BS with the generation of the second harmonics [see Figs. 10(d)–10(f)].

Further, we consider $\Omega = 2, k_L = 0$ with $v = 0$ which shows only the stable BS. As we quench $k_L = 0 \rightarrow 2$ and $\Omega = 2 \rightarrow 0$ the solitons repel each other [see Figs. 11(a)–11(c)]. Upon quenching the Rabi-coupling frequency from $\Omega = 2 \rightarrow 4$, we find that the soliton gets transformed into

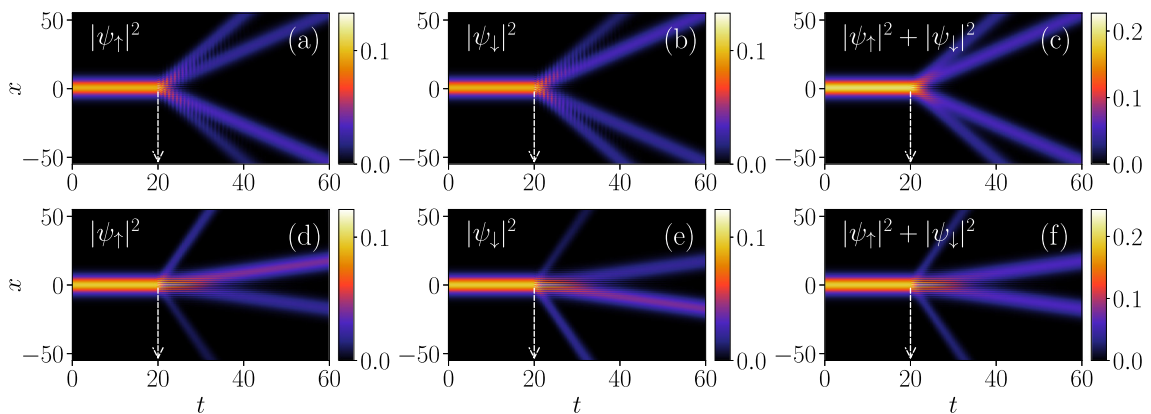


FIG. 9. Dynamics of the quantum soliton appearing due to different quenching protocols at $t = 20$ with $g = -g_{\uparrow\downarrow} = 0.5$ as it was initially prepared for $\Omega = 0, k_L = 2$. (a)–(c) When both Rabi frequency and SO coupling are quenched as $\Omega = 0 \rightarrow 50, k_L = 2 \rightarrow 4$ at $t = 20$, which results the transformation of nonmoving QBS soliton into moving multisoliton with large repulsion angle. (d)–(f) For quenching $\Omega = 0 \rightarrow 50, k_L = 2 \rightarrow 8$ at $t = 20$, QBS undergoes bifurcation into moving multisoliton state with small repulsive angle.

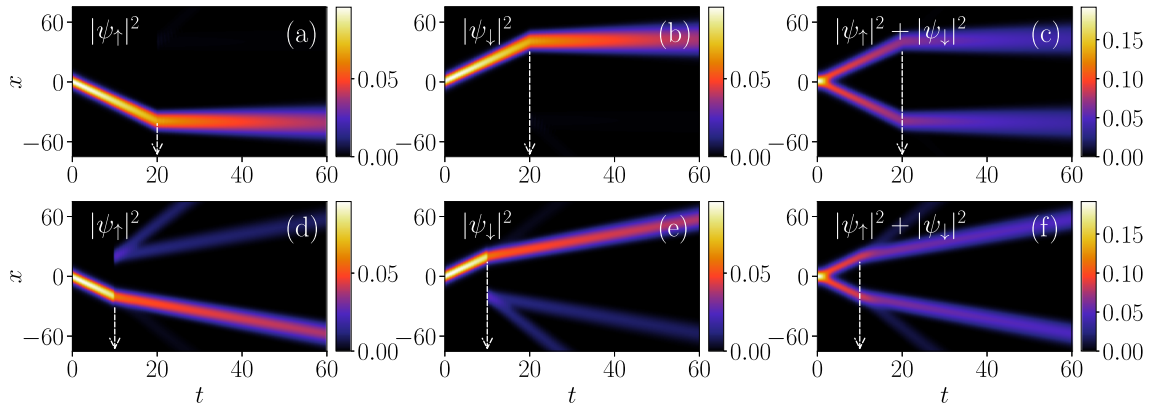


FIG. 10. Dynamics of the quantum soliton prepared with $g = -g_{\uparrow\downarrow} = 0.5$, $\Omega = 0$, and $k_L = 2$ appearing due to double-quenching protocols. (a)–(c) First quenching is performed at $t = 0$ with change in SO coupling ($k_L = 2 \rightarrow 0$) and second quenching is done at $t = 20$ when both coupling parameters are changed as $\Omega = 0 \rightarrow 1$ and $k_L = 0 \rightarrow 2$ which results as transforming the moving soliton to the stationary soliton. (d)–(f) At $t = 0$ first quenching is same as those in (a)–(c), while at $t = 10$ second quenching is done as $\Omega = 0 \rightarrow 5$ that results transforming the moving soliton into a soliton with secondary waves.

filaments after a finite time ($t \gtrsim 150$), which also appears to repel each other at ($t \gtrsim 250$) as depicted in Figs. 11(d)–11(f). The decay followed by the revival of the soliton along with multiple humps could be understood following the line of Ref. [34]. The main reason behind the fragmentation is the increase in the Rabi coupling while the change in the SO coupling triggers the movement of the soliton.

After discussing different dynamical behavior arising in the quantum bright soliton due to the quench of the coupling parameter in what follows, we present the related dynamics for the quantum stripe soliton. In Fig. 12, we depict the dynamics that arise due to the quenching of both coupling parameters when the ground state is quantum stripe soliton nature.

In Figs. 12(a)–12(c), we show the dynamics of soliton when quenching of both coupling parameters is performed at $t = 50$ for the initial state prepared with $g = -g_{\uparrow\downarrow} = 0.5$, $\Omega = 1$, $k_L = 2$. The quenching protocol for SO coupling is implemented as $k_L = 2 \rightarrow 0.2$, while for Rabi-coupling frequency, it is $\Omega = 1 \rightarrow 0.5$. We noticed that the quenching results in the bifurcation of stripe solitons into two parts wherein one shows weak breather soliton while the other

exhibits stronger behavior. Interestingly, here we find that the quenching leads to the excitation mode that exhibits the spin-flipping characteristics, which is quite evident from the dynamical change in the population in the spin-up and -down states in the alternate fashion with time. The observed spin flipping has been observed for the cases when Rabi coupling is quenched from the small ($\Omega < k_L^2$) to large ($\Omega > k_L^2$) value leading to the oscillatory instability. Similar observation has been made for the attractive binary mixture [34]. Note that the spin flipping can also be observed by making an imbalance in the atomic population of the condensate state at the initial time [39]. Further, the decrease of Rabi-coupling frequency leads to the disappearance of breathers and the generation of repulsive solitons. In Figs. 12(d)–12(f), we depict the dynamics of soliton when quenching of Rabi-coupling frequency is executed from $\Omega = 1 \rightarrow 2$ at $t = 20$. The quenching generates the stripe soliton breathers. Similar kinds of breathing solitons observed upon quenching the interaction strength so that the mean-field contribution becomes small in the binary mixture of the condensates [20].

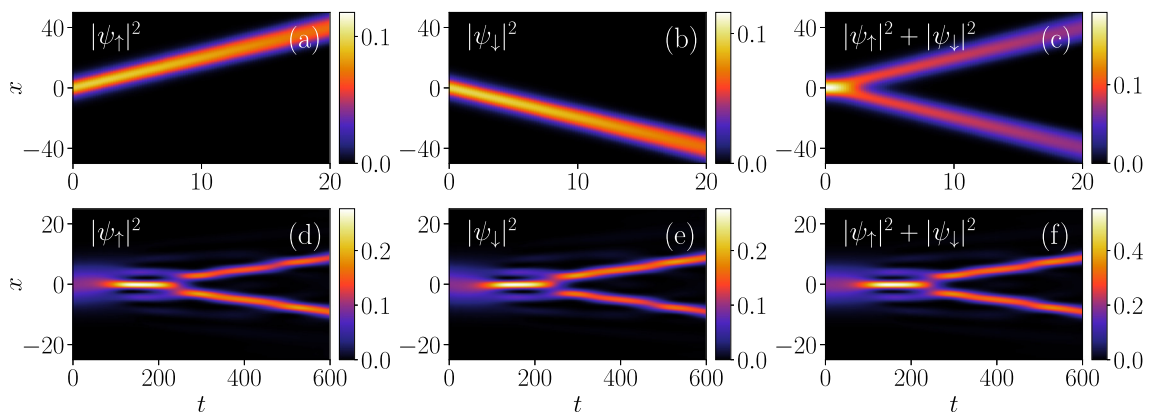


FIG. 11. Dynamics of the quantum BS soliton prepared with $g = -g_{\uparrow\downarrow} = 0.5$ and $\Omega = 2$, $k_L = 0$ as quenching of both the coupling parameters is performed. (a)–(c) Quenching is done as $k_L = 0 \rightarrow 2$, $\Omega = 2 \rightarrow 0$ that results the transition of bright soliton into moving soliton. (d)–(f) With quenching $k_L = 0 \rightarrow 2$, $\Omega = 2 \rightarrow 4$ breather soliton gets bifurcated into filament like soliton beyond $t \sim 250$.

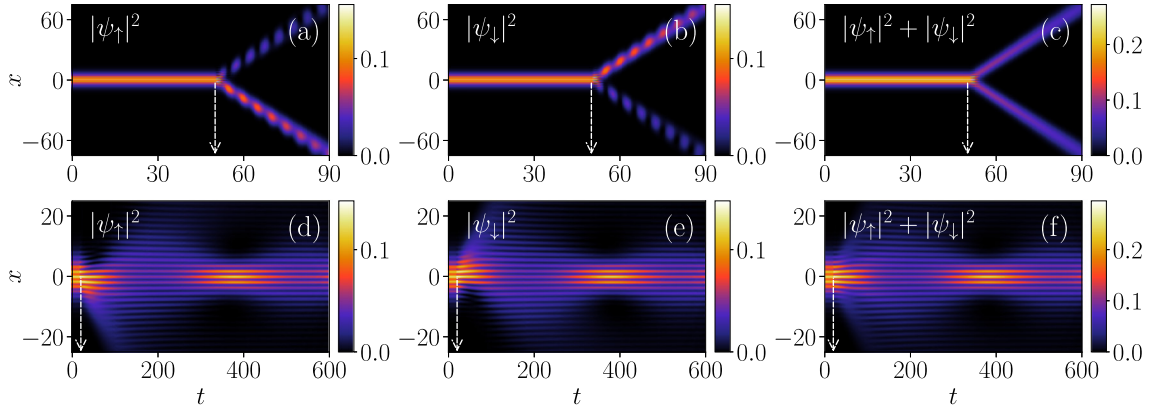


FIG. 12. Dynamics of the quantum stripe soliton prepared with $g = -g_{\uparrow\downarrow} = 0.5$ and $\Omega = 1$, $k_L = 2$ and the quenching is performed at finite time. (a)–(c) Quenching is performed as $k_L = 2 \rightarrow 0.2$, $\Omega = 1 \rightarrow 0.5$ at $t = 50$ that results the transition from the stripe soliton to the space-time breather bright soliton. (d)–(f) Quenching is performed as $\Omega = 1 \rightarrow 2$, $k_L = 2$ at $t = 20$ resulting in the transition from the stripe soliton to the breathing stripe soliton.

In Fig. 13, we show the dynamics that solely arises due to the quenching of the Rabi coupling for the ground states initially prepared for $g = -g_{\uparrow\downarrow} = 1.0$ and $\Omega = k_L = 2$. We quench the parameters as (a) $\Omega = 2 \rightarrow 1$ and (b) $\Omega = 2 \rightarrow 3$ at $t = 10$. Here we notice that the stripe soliton exhibits expansion upon the quenching of the parameters. We find that the breathing oscillation frequency increases on increasing the interaction strength, as shown in Fig. 6(c). Further, we consider another stripe soliton with $\Omega = k_L = 2$ in which the Rabi coupling is quenched as $\Omega = 2 \rightarrow 1$. For this, we find that the frequency of the striped soliton breather becomes $\omega_{\text{bf}} \sim 0.08$ upon increasing the interaction strength. When we change $\Omega = 2 \rightarrow 3$, we obtain that the initial profile, which has two maximum peaks and two side lobes, gets transformed into the multiple side lobes after the quench. Apart from this, the innermost soliton appears to repel each other after a finite time as they approach each other. A similar kind of dynamical behavior gets repeated over time.

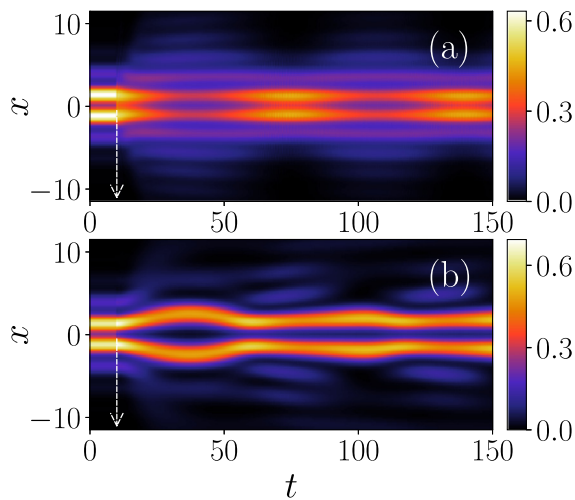


FIG. 13. Dynamics of quantum stripe soliton prepared with $g = -g_{\uparrow\downarrow} = 1.0$ and $\Omega = k_L = 2$ as the quenching is performed on the Rabi frequency at $t = 10$. (a) Soliton gets bifurcated into repulsive and attractive solitons as Rabi coupling is quenched as (a) $\Omega = 2 \rightarrow 1$ and (b) $\Omega = 2 \rightarrow 3$.

D. Collisional dynamics of quantum soliton

After studying the quenching dynamics of the quantum soliton by perturbing it with an initial velocity, in this section, we investigate how the solitons undergo different kinds of collisions that affect their overall stability depending upon the magnitude of the initial velocity. In particular, we find elastic, inelastic, repulsive, and space-time breather soliton against collisions.

In absence of the trap, the quantum solitons are set in motion by giving an initial velocity $\mp v$ to the stationary ground state $(\psi_{\uparrow}, \psi_{\downarrow})$ with a multiplier $\exp(\mp ivx)$, respectively [19]. Here we start for the case when the solitons are positioned at ± 50 for $g = -g_{\uparrow\downarrow} = 0.5$ and $\Omega = k_L = 0$. For a weak velocity ($v = 0.2$) the solitons undergo inelastic collision as depicted in Fig. 14(a). We find that the densities before the collision and after the collision are not the same. This indicates that after the collision, the solitons are unable to retain their shape and size same as those before the collision. As the initial positions of the soliton are at ± 50 the expected time for collision is $t = x/v = 250$ which can be clearly seen in Fig. 14(a). We find that after the collision ($t \sim 400$), the solitons start exhibiting the expansion, which makes them quite different in shape and size than they were before the collision. In order to understand the inelastic collision in a better way in Fig. 14(b) we plot the time evolution of the different energy contribution, like, kinetic energy (E_{ki}), mean-field energy (E_{mf}), LHY energy (E_{LHY}), and the total energy (E_T). The explicit form of energies is provided in the Eq. (A6) of Appendix A. We find that the mean-field, kinetic, LHY, and total energies after the collision do not remain same as they are before the collisions which is consistent with the inelastic nature of the collision observed in the classical case.

For large velocity ($v = 0.9$), we observe the elastic collision with no change in the shape of the soliton after the collision. In Fig. 14(c) we show the total density corresponding to the soliton when each component has been given an initial equal velocity ($v = 0.9$) but opposite direction with their initial positions at ± 50 for $g = -g_{\uparrow\downarrow} = 0.5$ and $\Omega = k_L = 0$. For this, the expected collision time will be at $t = 55.5$. We find that the densities before and after the collision are almost similar. In Fig. 14(d), we plot the time evolution of

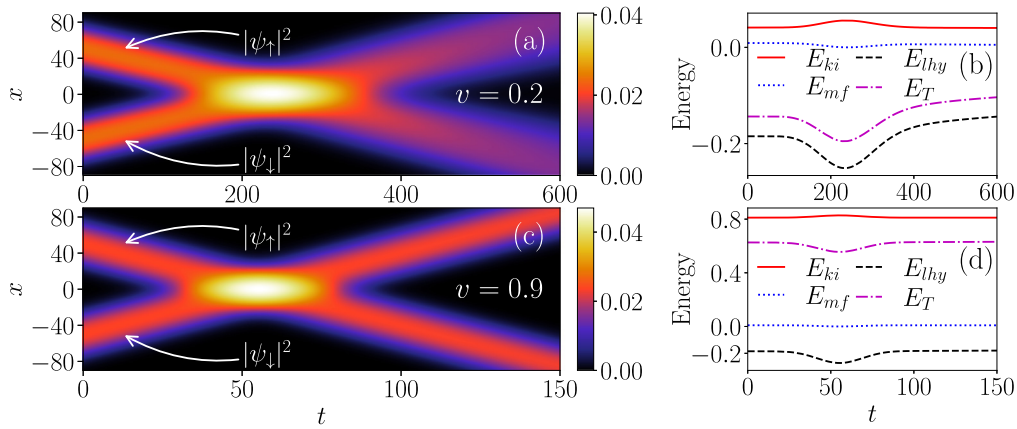


FIG. 14. (a) The total density plots depicting the inelastic collision dynamics between the quantum soliton for $g = -g_{\uparrow\downarrow} = 0.5$ and $\Omega = k_L = 0$ as the velocity given to the up and down components is in the direction of $-x$ and x , respectively, with magnitude $v = 0.2$. (b) Evolution of the different energies E_{ki} , E_{LHY} , E_{mf} , and total energy (E_T) with time for collision as shown in (a). There is a significant increase in the E_{LHY} and total energy (E_T) after the collision, indicating the inelastic nature of the same. (c) Plots of the total density depicting the elastic collision dynamics of quantum soliton for $v = 0.9$. (d) Evolution of the different energies with time for the collision as shown in (c). Before and after the collision, all the energy remains the same, indicating the elastic collision nature.

the different energy contributions to confirm the elastic nature of the collision. It is observed that the mean-field, kinetic, LHY, and total energies remain the same after the collisions than they were before the collision, which are consistent with the elastic nature of the collision. This behavior is consistent with the experimental observations of the collision between the quantum droplet in three dimensions [15]. Note that similar feature of the collision between the quantum droplets has been reported for the symmetric components of the binary mixture with finite interaction [19]. So far, we have analyzed the collisional dynamics of the binary BECs with LHY correction and in the absence of Rabi- and SO-coupling parameters. However, as we consider it for finite SO and Rabi couplings, we find that the solitons get degenerated and, thus, it could not provide the relevant collision dynamics. Considering what follows, we present the collision dynamics by keeping either SO- or Rabi-coupling frequency to be finite. Here as we obtain the spatially separated soliton, we employ the quenching of velocity and the coupling parameter, which was zero while

preparing the states. To study the collisional dynamics with finite coupling parameters, we prepare the initial ground state with $\Omega = 1$ and $k_L = 0$. For this case, we find each spin component degenerates in the $\pm x$ direction and further exhibits the space-time breathers, which experience expansion after the finite time ($t \sim 40$). As we pass on the finite velocity, the solitons start interacting with each other. As for an example, for $v = 1$ the soliton starts moving towards each other that results in the elastic collision between them at $t \sim 20$. Note that here, after the collision, there is a small change in the density, which is different from the collision behavior observed in Fig. 14(c). Therefore, we refer to this as the quasielastic collision. To avoid the repetition of depiction of the typical solitonic behavior (like, space-time breathers and quasielastic collision) here we have not given any figure corresponding to this observation.

Next, we present the collisional dynamics by preparing the ground states with finite SO-coupling and zero Rabi-coupling frequencies. We consider the system with $\Omega = 0$,

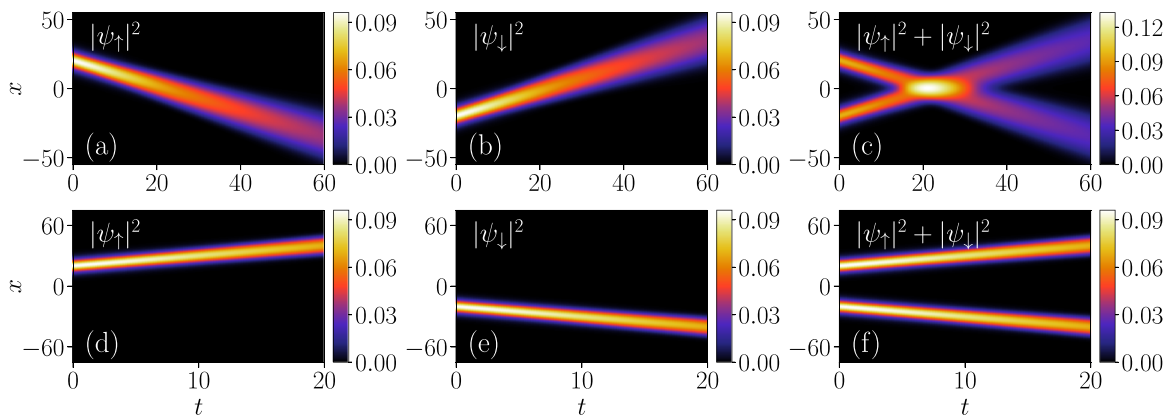


FIG. 15. Collisional dynamics of the quantum solitons prepared with $g = -g_{\uparrow\downarrow} = 0.5$, $\Omega = 0$ and $k_L = 0.5$ and the individual components are given equal and opposite velocity ($v = 0.5$) at $t = 0$. Also, quenching on SO coupling parameter is performed as (a)–(c) $k_L = 0.5 \rightarrow 0.1$ and (d)–(f) $k_L = 0.5 \rightarrow 2$. Upon quenching the SO coupling, the solitons undergo inelastic collision in (a)–(c), while solitons repel each other for (d)–(f).

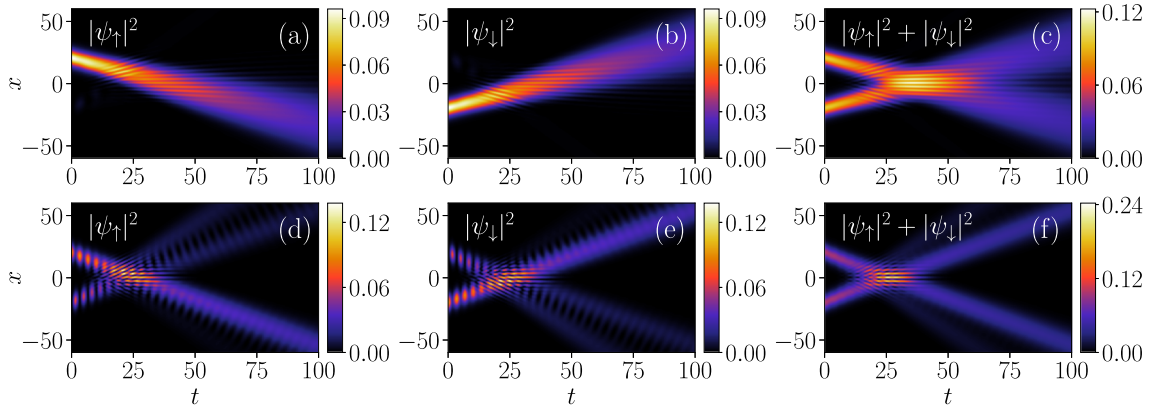


FIG. 16. Collisional dynamics of the quantum solitons prepared with the same parameters and given same velocity at $t = 0$ as those for Fig. 15. At $t = 0$ the Rabi coupling is quenched as (a)–(c) $\Omega = 0 \rightarrow 0.1$, (d)–(f) $\Omega = 0 \rightarrow 0.8$. Upon quenching, the Rabi-coupling quantum soliton undergoes inelastic collision and displays an interference pattern (a)–(c). However, the soliton displays quasielastic collision with secondary solitons generation in (d)–(f).

$k_L = 0.5$ with $g = 0.5$ and finite velocity $v = 0.5$. Once we prepare the ground state, we analyze the collisional dynamics by quenching the SO coupling for two different situations. When $v > k_L/2$, the nondegenerated soliton with decaying or expansion feature undergoes inelastic collision as depicted in Figs. 15(a)–15(c). However, for $v < k_L/2$ we observe that the soliton appears to repel each other upon progression of time [see Figs. 15(d)–15(f)].

Further, we analyze the collision dynamics by quenching the Rabi coupling. Like in the previous case, we study the dynamics of the solitons for two different situations. When $\Omega < k_L^2$ the nondegenerated soliton undergoes inelastic collision. They appear to show the stripe fringes as depicted in Figs. 16(a)–16(c). For $\Omega > k_L^2$, we find a collision of bright soliton is quasielastic with the generation of interference stripe fringes. We also witness the generation of secondary solitons, as shown in Figs. 16(d)–16(f).

V. SUMMARY AND CONCLUSIONS

Using the mean-field model along with the LHY correction, we have numerically investigated the structure and dynamics of the ground state of the self-bound state in 1D spin-orbit-coupled BECs. Depending upon the nature of Rabi and SO couplings, the ground state is either quantum bright or stripe soliton. We deduced an analytical solution of the quantum bright soliton without Rabi coupling. We further studied the dynamics of the soliton using the three protocols, namely, by giving the initial velocity to the soliton, quenching the SO and Rabi coupling parameters, and allowing the component to collide by attributing an equal and opposite initial velocity. We found that the velocity perturbations generate breathinglike soliton. The breathing frequency increases upon the increase in the SO coupling for a given Rabi coupling frequency attains a maximum at the SO coupling, where the phase transition from the quantum bright to stripe soliton takes place. The magnitude of breathing frequency at critical SO coupling remains independent of the initial velocity and exhibits a power-law dependence on the Rabi-coupling frequency with an exponent ~ 0.16 . We found that the critical breathing frequency increases upon increasing the interaction strengths.

Using the contribution of the kinetic, SO, and Rabi energy terms, we find that while domination of the breathing soliton phase by the SO and Rabi couplings, the moving soliton phase is the result of the kinetic energy part. This particular feature leads the attainment of the minima of the chemical potential at the critical velocity where change in the phase takes place. We have realized the presence of several dynamical phase transitions, like QBS to QSS and the multisoliton behavior depending upon the quenching protocol of the Rabi-coupling parameters. By quenching both Rabi and SO couplings, we can control the direction and angle of the inner and outer solitons. The quenching of Rabi and SO couplings facilitates several interesting dynamical phases like a repulsive soliton, space-time breathers, filamentation, etc.

We have also analyzed the collision dynamics of solitons. Depending upon the velocity of the soliton, we observed the presence of elastic and inelastic collisions. An inelastic collision occurs for low velocities, while it exhibits elastic collision at high velocities consistent with earlier experimental observations [15]. We have also complemented the collision dynamics by analyzing the nature of different energy terms like kinetic energy, mean-field energy, and LHY. Also, we analyzed the collision dynamics of the solitons by quenching either the velocity or the SO and Rabi couplings. For the former, we found the presence of quasielastic collision, while for the latter, we realize inelastic collision.

In this paper, we have considered the dynamical evolution of the quantum solitons for the situation when the mean-field contribution is negligible. It would be interesting to explore the dynamics in the similar line presented in this work in the presence of significant mean-field contribution along with the LHY correction in the quantum soliton.

ACKNOWLEDGMENTS

We thank C. Cabrera for his comments on the initial draft of our manuscript. S.G. would like to acknowledge the financial support from the University Grants Commission, Council of Scientific and Industrial Research (UGC-CSIR), India. R.R. acknowledges support from the Ministry of Science and Technology (MOST), Taiwan, under Grant No. MOST-111-

2119-M-001-002. P.K.M. acknowledges the Department of Science and Technology, Science and Engineering Research Board (DST-SERB), India, for the financial support through Project No. ECR/2017/002639. The work of P.M. is supported by DST-SERB under Grant No. CRG/2019/004059, DST-FIST under Grant No. SR/FST/PSI-204/2015(C), and MoE RUSA 2.0 (Physical Sciences).

APPENDIX: CALCULATION OF ENERGY IN THE SO-COUPLED BECs WITH LHY CORRECTION

In this Appendix, we provide the detailed steps to obtain the total energy of the SO-coupled BECs with LHY correc-

tion. The stationary state solution is given by

$$\psi_j(x, y) = (\psi_{jR} + i\psi_{jI})e^{-i\mu_j t}, \quad (\text{A1})$$

where $j \in \{\uparrow, \downarrow\}$, ψ_{jR} and ψ_{jI} are the real and imaginary parts of the stationary wave function, respectively, and $\mu_{\uparrow, \downarrow}$ are the chemical potential of the spin-up and -down components, respectively [40]. As we insert this solution in Eqs. (1) we get

$$\mu_{\uparrow}\psi_{\uparrow R} = \left[-\frac{1}{2}\frac{\partial^2}{\partial x^2} + g|\psi_{\uparrow}|^2 + g_{\uparrow\downarrow}|\psi_{\downarrow}|^2 - \frac{g^{3/2}}{\pi}\sqrt{|\psi_{\uparrow}|^2 + |\psi_{\downarrow}|^2} \right] \psi_{\uparrow R} + k_L \left(\frac{\partial\psi_{\uparrow I}}{\partial x} \right) + \Omega\psi_{\downarrow R}, \quad (\text{A2a})$$

$$\mu_{\downarrow}\psi_{\downarrow R} = \left[-\frac{1}{2}\frac{\partial^2}{\partial x^2} + g|\psi_{\downarrow}|^2 + g_{\uparrow\downarrow}|\psi_{\uparrow}|^2 - \frac{g^{3/2}}{\pi}\sqrt{|\psi_{\uparrow}|^2 + |\psi_{\downarrow}|^2} \right] \psi_{\downarrow R} - k_L \left(\frac{\partial\psi_{\downarrow I}}{\partial x} \right) + \Omega\psi_{\uparrow R}, \quad (\text{A2b})$$

and for the imaginary parts we have

$$\mu_{\uparrow}\psi_{\uparrow I} = \left[-\frac{1}{2}\frac{\partial^2}{\partial x^2} + g|\psi_{\uparrow}|^2 + g_{\uparrow\downarrow}|\psi_{\downarrow}|^2 - \frac{g^{3/2}}{\pi}\sqrt{|\psi_{\uparrow}|^2 + |\psi_{\downarrow}|^2} \right] \psi_{\uparrow I} - k_L \left(\frac{\partial\psi_{\uparrow R}}{\partial x} \right) + \Omega\psi_{\downarrow I}, \quad (\text{A2c})$$

$$\mu_{\downarrow}\psi_{\downarrow I} = \left[-\frac{1}{2}\frac{\partial^2}{\partial x^2} + g|\psi_{\downarrow}|^2 + g_{\uparrow\downarrow}|\psi_{\uparrow}|^2 - \frac{g^{3/2}}{\pi}\sqrt{|\psi_{\uparrow}|^2 + |\psi_{\downarrow}|^2} \right] \psi_{\downarrow I} + k_L \left(\frac{\partial\psi_{\downarrow R}}{\partial x} \right) + \Omega\psi_{\uparrow I}, \quad (\text{A2d})$$

where $|\psi_{\uparrow}|^2 = \psi_{\uparrow R}^2 + \psi_{\uparrow I}^2$ and $|\psi_{\downarrow}|^2 = \psi_{\downarrow R}^2 + \psi_{\downarrow I}^2$. Multiplying Eq. (A2a) with $\psi_{\uparrow R}$ and Eq. (A2b) with $\psi_{\downarrow R}$, and integrating we get

$$\mu_{\uparrow} \int dx \psi_{\uparrow R}^2 = \int dx \psi_{\uparrow R} \left\{ \left[-\frac{1}{2}\frac{\partial^2}{\partial x^2} + g|\psi_{\uparrow}|^2 + g_{\uparrow\downarrow}|\psi_{\downarrow}|^2 - \frac{g^{3/2}}{\pi}\sqrt{|\psi_{\uparrow}|^2 + |\psi_{\downarrow}|^2} \right] \psi_{\uparrow R} + k_L \left(\frac{\partial\psi_{\uparrow I}}{\partial x} \right) + \Omega\psi_{\downarrow R} \right\}, \quad (\text{A3a})$$

$$\mu_{\downarrow} \int dx \psi_{\downarrow R}^2 = \int dx \psi_{\downarrow R} \left\{ \left[-\frac{1}{2}\frac{\partial^2}{\partial x^2} + g|\psi_{\downarrow}|^2 + g_{\uparrow\downarrow}|\psi_{\uparrow}|^2 - \frac{g^{3/2}}{\pi}\sqrt{|\psi_{\uparrow}|^2 + |\psi_{\downarrow}|^2} \right] \psi_{\downarrow R} - k_L \left(\frac{\partial\psi_{\downarrow I}}{\partial x} \right) + \Omega\psi_{\uparrow R} \right\}. \quad (\text{A3b})$$

Similarly, from the imaginary-part equations [Eqs. (A2c) and (A2d)] we obtain

$$\mu_{\uparrow} \int dx \psi_{\uparrow I}^2 = \int dx \psi_{\uparrow I} \left\{ \left[-\frac{1}{2}\frac{\partial^2}{\partial x^2} + g|\psi_{\uparrow}|^2 + g_{\uparrow\downarrow}|\psi_{\downarrow}|^2 - \frac{g^{3/2}}{\pi}\sqrt{|\psi_{\uparrow}|^2 + |\psi_{\downarrow}|^2} \right] \psi_{\uparrow I} - k_L \left(\frac{\partial\psi_{\uparrow R}}{\partial x} \right) + \Omega\psi_{\downarrow I} \right\}, \quad (\text{A4a})$$

$$\mu_{\downarrow} \int dx \psi_{\downarrow I}^2 = \int dx \psi_{\downarrow I} \left\{ \left[-\frac{1}{2}\frac{\partial^2}{\partial x^2} + g|\psi_{\downarrow}|^2 + g_{\uparrow\downarrow}|\psi_{\uparrow}|^2 - \frac{g^{3/2}}{\pi}\sqrt{|\psi_{\uparrow}|^2 + |\psi_{\downarrow}|^2} \right] \psi_{\downarrow I} + k_L \left(\frac{\partial\psi_{\downarrow R}}{\partial x} \right) + \Omega\psi_{\uparrow I} \right\}. \quad (\text{A4b})$$

Upon rearranging the above equations [Eqs. (A3b)–(A4b)] we obtain

$$\begin{aligned} \mu_{\uparrow} = & \frac{1}{\int |\psi_{\uparrow}|^2 dx} \int \left[\frac{1}{2} \left| \frac{\partial\psi_{\uparrow}}{\partial x} \right|^2 + \left\{ g|\psi_{\uparrow}|^2 + g_{\uparrow\downarrow}|\psi_{\downarrow}|^2 - \frac{g^{3/2}}{\pi}\sqrt{|\psi_{\uparrow}|^2 + |\psi_{\downarrow}|^2} \right\} |\psi_{\uparrow}|^2 \right] dx \\ & + \frac{1}{\int |\psi_{\uparrow}|^2 dx} \int \left[k_L \left(\frac{\partial\psi_{\uparrow I}}{\partial x} \right) + \Omega\psi_{\downarrow R} \right] \psi_{\uparrow R} dx + \frac{1}{\int |\psi_{\uparrow}|^2 dx} \int \left[-k_L \left(\frac{\partial\psi_{\uparrow R}}{\partial x} \right) + \Omega\psi_{\downarrow I} \right] \psi_{\uparrow I} dx, \end{aligned} \quad (\text{A5a})$$

$$\begin{aligned} \mu_{\downarrow} = & \frac{1}{\int |\psi_{\downarrow}|^2 dx} \int \left[\frac{1}{2} \left| \frac{\partial\psi_{\downarrow}}{\partial x} \right|^2 + \left\{ g|\psi_{\downarrow}|^2 + g_{\uparrow\downarrow}|\psi_{\uparrow}|^2 - \frac{g^{3/2}}{\pi}\sqrt{|\psi_{\uparrow}|^2 + |\psi_{\downarrow}|^2} \right\} |\psi_{\downarrow}|^2 \right] dx \\ & + \frac{1}{\int |\psi_{\downarrow}|^2 dx} \int \left[-k_L \left(\frac{\partial\psi_{\downarrow I}}{\partial x} \right) + \Omega\psi_{\uparrow R} \right] \psi_{\downarrow R} dx + \frac{1}{\int |\psi_{\downarrow}|^2 dx} \int \left[k_L \left(\frac{\partial\psi_{\downarrow R}}{\partial x} \right) + \Omega\psi_{\uparrow I} \right] \psi_{\downarrow I} dx. \end{aligned} \quad (\text{A5b})$$

From the above equations we obtain the different contribution in the energy as

$$E_{\text{ki}} = \int \left[\frac{1}{2\int |\psi_{\uparrow}|^2 dx} \left| \frac{\partial\psi_{\uparrow}}{\partial x} \right|^2 + \frac{1}{2\int |\psi_{\downarrow}|^2 dx} \left| \frac{\partial\psi_{\downarrow}}{\partial x} \right|^2 \right] dx, \quad (\text{A6a})$$

$$E_{\text{mf}} = \int \left[\frac{1}{\int |\psi_{\uparrow}|^2 dx} \left[\frac{g}{2} |\psi_{\uparrow}|^2 + \frac{g_{\downarrow\uparrow}}{2} |\psi_{\downarrow}|^2 \right] |\psi_{\uparrow}|^2 + \frac{1}{\int |\psi_{\downarrow}|^2 dx} \left[\frac{g_{\downarrow\uparrow}}{2} |\psi_{\uparrow}|^2 + \frac{g}{2} |\psi_{\downarrow}|^2 \right] |\psi_{\downarrow}|^2 \right] dx, \quad (\text{A6b})$$

$$E_{\text{LHY}} = \int \left[-\frac{1}{\int |\psi_{\uparrow}|^2 dx} \left[\frac{2}{3\pi} g^{3/2} \sqrt{|\psi_{\uparrow}|^2 + |\psi_{\downarrow}|^2} \right] |\psi_{\uparrow}|^2 - \frac{1}{\int |\psi_{\downarrow}|^2 dx} \left[\frac{2}{3\pi} g^{3/2} \sqrt{|\psi_{\uparrow}|^2 + |\psi_{\downarrow}|^2} \right] |\psi_{\downarrow}|^2 \right] dx, \quad (\text{A6c})$$

$$E_{\text{SO}} = \int \left\{ \frac{1}{\int |\psi_{\uparrow}|^2 dx} \left[\left(k_L \frac{\partial \psi_{\uparrow I}}{\partial x} \right) \psi_{\uparrow R} + \left(-k_L \frac{\partial \psi_{\uparrow R}}{\partial x} \right) \psi_{\uparrow I} \right] + \frac{1}{\int |\psi_{\downarrow}|^2 dx} \left[\left(-k_L \frac{\partial \psi_{\downarrow I}}{\partial x} \right) \psi_{\downarrow R} + \left(k_L \frac{\partial \psi_{\downarrow R}}{\partial x} \right) \psi_{\downarrow I} \right] \right\} dx, \quad (\text{A6d})$$

$$E_{\text{Rabi}} = \int \left\{ \frac{1}{\int |\psi_{\uparrow}|^2 dx} [(\Omega \psi_{\downarrow R}) \psi_{\uparrow R} + (\Omega \psi_{\downarrow I}) \psi_{\uparrow I}] + \frac{1}{\int |\psi_{\downarrow}|^2 dx} [(\Omega \psi_{\uparrow R}) \psi_{\downarrow R} + (\Omega \psi_{\uparrow I}) \psi_{\downarrow I}] \right\} dx, \quad (\text{A6e})$$

where E_{ki} represents the kinetic energy, E_{mf} mean-field contribution, E_{LHY} is the energy due to the LHY correction, and E_{SO} is the contribution due to the SO coupling. The total energy $E_T = E_{\text{ki}} + E_{\text{mf}} + E_{\text{LHY}} + E_{\text{SO}}$.

-
- [1] D. S. Petrov, *Phys. Rev. Lett.* **115**, 155302 (2015).
[2] D. S. Petrov and G. E. Astrakharchik, *Phys. Rev. Lett.* **117**, 100401 (2016).
[3] Z.-H. Luo, W. Pang, B. Liu, Y.-Y. Li, and B. A. Malomed, *Front. Phys.* **16**, 32201 (2021).
[4] T. D. Lee, K. Huang, and C. N. Yang, *Phys. Rev.* **106**, 1135 (1957).
[5] S. B. Papp, J. M. Pino, R. J. Wild, S. Ronen, C. E. Wieman, D. S. Jin, and E. A. Cornell, *Phys. Rev. Lett.* **101**, 135301 (2008).
[6] N. Navon, S. Piatecki, K. Günter, B. Rem, T. C. Nguyen, F. Chevy, W. Krauth, and C. Salomon, *Phys. Rev. Lett.* **107**, 135301 (2011).
[7] T. G. Skov, M. G. Skou, N. B. Jørgensen, and J. J. Arlt, *Phys. Rev. Lett.* **126**, 230404 (2021).
[8] I. Ferrier-Barbut, H. H. Kadau, M. Schmitt, M. Wenzel, and T. Pfau, *Phys. Rev. Lett.* **116**, 215301 (2016).
[9] M. Schmitt, M. Wenzel, F. Böttcher, I. Ferrier-Barbut, and T. Pfau, *Nature (London)* **539**, 259 (2016).
[10] I. Ferrier-Barbut, M. Schmitt, M. Wenzel, H. Kadau, and T. Pfau, *J. Phys. B: At. Mol. Opt. Phys.* **49**, 214004 (2016).
[11] L. Chomaz, S. Baier, D. Petter, M. J. Mark, F. Wächtler, L. Santos, and F. Ferlaino, *Phys. Rev. X* **6**, 041039 (2016).
[12] C. R. Cabrera, L. Tanzi, J. Sanz, B. Naylor, P. Thomas, P. Cheiney, and L. Tarruell, *Science* **359**, 301 (2018).
[13] P. Cheiney, C. R. Cabrera, J. Sanz, B. Naylor, L. Tanzi, and L. Tarruell, *Phys. Rev. Lett.* **120**, 135301 (2018).
[14] G. Semeghini, G. Ferioli, L. Masi, C. Mazzinghi, L. Wolswijk, F. Minardi, M. Modugno, G. Modugno, M. Inguscio, and M. Fattori, *Phys. Rev. Lett.* **120**, 235301 (2018).
[15] G. Ferioli, G. Semeghini, L. Masi, G. Giusti, G. Modugno, M. Inguscio, A. Gallemi, A. Recati, and M. Fattori, *Phys. Rev. Lett.* **122**, 090401 (2019).
[16] D. Rakshit, T. Karpiuk, M. Brewczyk, and M. Gajda, *SciPost Phys.* **6**, 079 (2019).
[17] J. C. Smith, D. Baillie, and P. B. Blakie, *Phys. Rev. Lett.* **126**, 025302 (2021).
[18] A. Frölian, C. S. Chisholm, E. Neri, C. R. Cabrera, R. Ramos, A. Celi, and L. Tarruell, *Nature (London)* **608**, 293 (2022).
[19] G. E. Astrakharchik and B. A. Malomed, *Phys. Rev. A* **98**, 013631 (2018).
[20] S. I. Mistakidis, T. Mithun, P. G. Kevrekidis, H. R. Sadeghpour, and P. Schmelcher, *Phys. Rev. Res.* **3**, 043128 (2021).
[21] A. Tononi, Y. Wang, and L. Salasnich, *Phys. Rev. A* **99**, 063618 (2019).
[22] S. Sahu and D. Majumdar, *J. Phys. B: At. Mol. Opt. Phys.* **53**, 095301 (2020).
[23] E. Chiquillo, *Phys. Rev. A* **97**, 013614 (2018).
[24] M. R. Pathak and A. Nath, *Sci. Rep.* **12**, 6904 (2022).
[25] Y. Li, Z. Luo, Y. Liu, Z. Chen, C. Huang, S. Fu, H. Tan, and B. A. Malomed, *New J. Phys.* **19**, 113043 (2017).
[26] K.-L. Pan, C. K. Law, K. Chung, and B. Zhou, *J. Appl. Phys.* **103**, 064901 (2008).
[27] L. E. Young-S. and S. K. Adhikari, *Commun. Nonlinear Sci. Numer. Simul.* **106**, 106094 (2022).
[28] Y. J. Lin, K. Jimenez-Garcia, and I. Spielman, *Nature (London)* **471**, 83 (2011).
[29] P. Muruganandam, and S. K. Adhikari, *Comput. Phys. Commun.* **180**, 1888 (2009).
[30] L. E. Young-S., D. Vudragović, P. Muruganandam, S. K. Adhikari, and A. Balaž, *Comput. Phys. Commun.* **204**, 209 (2016).
[31] R. Ravisankar, D. Vudragović, P. Muruganandam, A. Balaž, and S. K. Adhikari, *Comput. Phys. Commun.* **259**, 107657 (2021).
[32] R. Ravisankar, T. Sriraman, and P. Muruganandam, in *AIP Conference Proceedings*, Vol. 2265 (AIP, Melville, NY, 2020), p. 030022.
[33] J. Denschlag, J. E. Simsarian, D. L. Feder, C. W. Clark, L. A. Collins, J. Cubizolles, L. Deng, E. W. Hagley, K. Helmerson, W. P. Reinhardt *et al.*, *Science* **287**, 97 (2000).
[34] R. Ravisankar, T. Sriraman, L. Salasnich, and P. Muruganandam, *J. Phys. B: At. Mol. Opt. Phys.* **53**, 195301 (2020).
[35] A. Di Carli, C. D. Colquhoun, G. Henderson, S. Flannigan, G. L. Oppo, A. J. Daley, S. Kuhr, and E. Haller, *Phys. Rev. Lett.* **123**, 123602 (2019).
[36] C. Li, C. Qu, R. J. Niffenegger, S. Wang, M. He, D. B. Blasing, A. J. Olson, C. H. Greene, Y. Lyanda-Geller, Q. Zhou *et al.*, *Nat. Commun.* **10**, 375 (2019).
[37] S. Mardonov, M. Modugno, and E. Y. Sherman, *J. Phys. B: At. Mol. Opt. Phys.* **48**, 115302 (2015).
[38] R. Ravisankar, T. Sriraman, R. K. Kumar, P. Muruganandam, and P. K. Mishra, *J. Phys. B: At. Mol. Opt. Phys.* **54**, 225301 (2021).
[39] Y. Cheng, G. Tang, and S. K. Adhikari, *Phys. Rev. A* **89**, 063602 (2014).
[40] R. Ravisankar, H. Fabrelli, A. Gammal, P. Muruganandam, and P. K. Mishra, *Phys. Rev. A* **104**, 053315 (2021).